PHYSICS

Phonon localization in heat conduction

M. N. Luckyanova[1], J. Mendoza[1], H. Lu[2]*, B. Song[1], S. Huang[3]†, J. Zhou[1], M. Li[1]‡, Y. Dong[4,5], H. Zhou[4], J. Garlow[6]§, L. Wu[6], B. J. Kirby[7], A. J. Grutter[7], A. A. Puretzky[8], Y. Zhu[6], M. S. Dresselhaus[3,9], A. Gossard[2], G. Chen[1]||

Nondiffusive phonon thermal transport, extensively observed in nanostructures, has largely been attributed to classical size effects, ignoring the wave nature of phonons. We report localization behavior in phonon heat conduction due to multiple scattering and interference events of broadband phonons, by measuring the thermal conductivities of GaAs/AlAs superlattices with ErAs nanodots randomly distributed at the interfaces. With an increasing number of superlattice periods, the measured thermal conductivities near room temperature increased and eventually saturated, indicating a transition from ballistic to diffusive transport. In contrast, at cryogenic temperatures the thermal conductivities first increased but then decreased, signaling phonon wave localization, as supported by atomistic Green's function simulations. The discovery of phonon localization suggests a new path forward for engineering phonon thermal transport.

INTRODUCTION

The phonons responsible for heat conduction in most dielectrics and semiconductors have short wavelengths. Although studies of phonon heat conduction in nanostructures over the past two decades have demonstrated the presence of strong size effects, most experimental observations of the departure from bulk behavior can be explained without invoking the wave nature of phonons (1). Instead, the classical size effects happen when the phonon mean free paths (MFPs) are longer than the characteristic lengths of the structures, and these effects are important for a wide range of applications including thermoelectric energy conversion and microelectronic thermal management (2–6). The potential of engineering phonon heat conduction via wave effects such as bandgap formation (7–9), solitons (10), or localization (11, 12) has been suggested before, but conclusive experiments have been lacking until recent demonstrations of coherent phonon heat conduction (13, 14) in superlattices (SLs). Previous simulations and recent experiments revealed that, in SLs, most phonons responsible for heat conduction have relatively long wavelengths because short-wavelength phonons are strongly scattered by atomic mixing at individual interfaces (13, 15–17). These long-wavelength phonons maintain their phases while propagating through multiple periods and even the entire thickness of an SL. If these phonons can be effectively scattered, then the thermal conductivity of an SL will be further reduced. Here, we demonstrate the ability to control the mid- to long-wavelength phonons by placing nanoscale dots at the internal interfaces of SLs, leading to a further reduction of SL thermal conductivity by over a factor of two. Furthermore, our experiments and simulations reveal that the embedded nanodots cause phonon localization over a broad frequency range, establishing a new paradigm for engineering phonon heat conduction in solids.

In an SL system, high-frequency phonons are substantially scattered by interface roughness and atomic mixing. Since the length scale of interface roughness is usually too small to effectively scatter long-wavelength phonons, they are instead dominantly scattered through anharmonic processes (13). When the MFPs of these low-frequency phonons are longer than the entire sample thickness, they are scattered at the outer boundaries of the SLs rather than at the internal interfaces. These propagating phonons represent eigenstates of the SL rather than of the parent materials. Such coherent phonon transport has been previously observed in GaAs/AlAs SLs, where the period thickness was held constant while the number of periods, and thus the overall sample thickness, was varied (13). The thermal conductivity of these SLs depends on the total thickness. This effect was especially pronounced at lower temperatures, where long-wavelength phonons dominate thermal transport. By introducing scatterers with sizes comparable to the wavelengths of these phonons, further reduction in the thermal conductivity is expected. Moreover, it was predicted that scattering centers randomly distributed at the interfaces of SLs may lead to photon localization (18). It will be especially interesting to see whether coherent phonons in the SLs can be localized in a similar configuration.

RESULTS

Experimental evidence of localization

We fabricated three sets of seven GaAs/AlAs SLs with 4, 8, 12, 16, 100, 200, and 300 periods each comprising a 3-nm GaAs layer and a 3-nm AlAs layer on a semi-insulating GaAs (001) substrate (see Materials and Methods for details). The three sets of SLs are distinguished by the density of ErAs nanodots (diameter, ~3 nm) epitaxially grown at the interfaces of the GaAs and AlAs layers: (i) a reference set without dots, (ii) a set with ErAs dots covering 8% of the interface area and a spacing of about 9.5 nm between the dots, and (iii) a set with 25% interface coverage and an interdot spacing of 5.5 nm. A schematic of the SLs and transmission electron microscopy (TEM) images of representative samples are shown in Fig. 1 (also in figs. S1 and S2). The images confirm

[1]Department of Mechanical Engineering, Massachusetts Institute of Technology, Cambridge, MA 02139, USA. [2]Materials Department, University of California, Santa Barbara, Santa Barbara, CA 93106, USA. [3]Department of Electrical Engineering and Computer Science, Massachusetts Institute of Technology, Cambridge, MA 02139, USA. [4]Advanced Photon Source, Argonne National Laboratory, Argonne, IL 60439, USA. [5]National Synchrotron Radiation Laboratory, University of Science and Technology of China, Hefei, Anhui 230026, China. [6]Condensed Matter Physics and Materials Science Department, Brookhaven National Laboratory, Upton, NY 11973, USA. [7]Center for Neutron Research, National Institute of Standards and Technology, Gaithersburg, MD 20899, USA. [8]Center for Nanophase Materials Science, Oak Ridge National Laboratory, Oak Ridge, TN 37831, USA. [9]Department of Physics, Massachusetts Institute of Technology, Cambridge, MA 02139, USA.
*Present address: College of Engineering and Applied Sciences, Nanjing University, Nanjing 210093, China.
†Present address: Department of Electrical Engineering, Pennsylvania State University, University Park, PA 16802, USA.
‡Present address: Department of Nuclear Science and Engineering, Massachusetts Institute of Technology, Cambridge, MA 02139, USA.
§Present address: Department of Materials Science and Chemical Engineering, Stony Brook University, Stony Brook, NY 11794, USA.
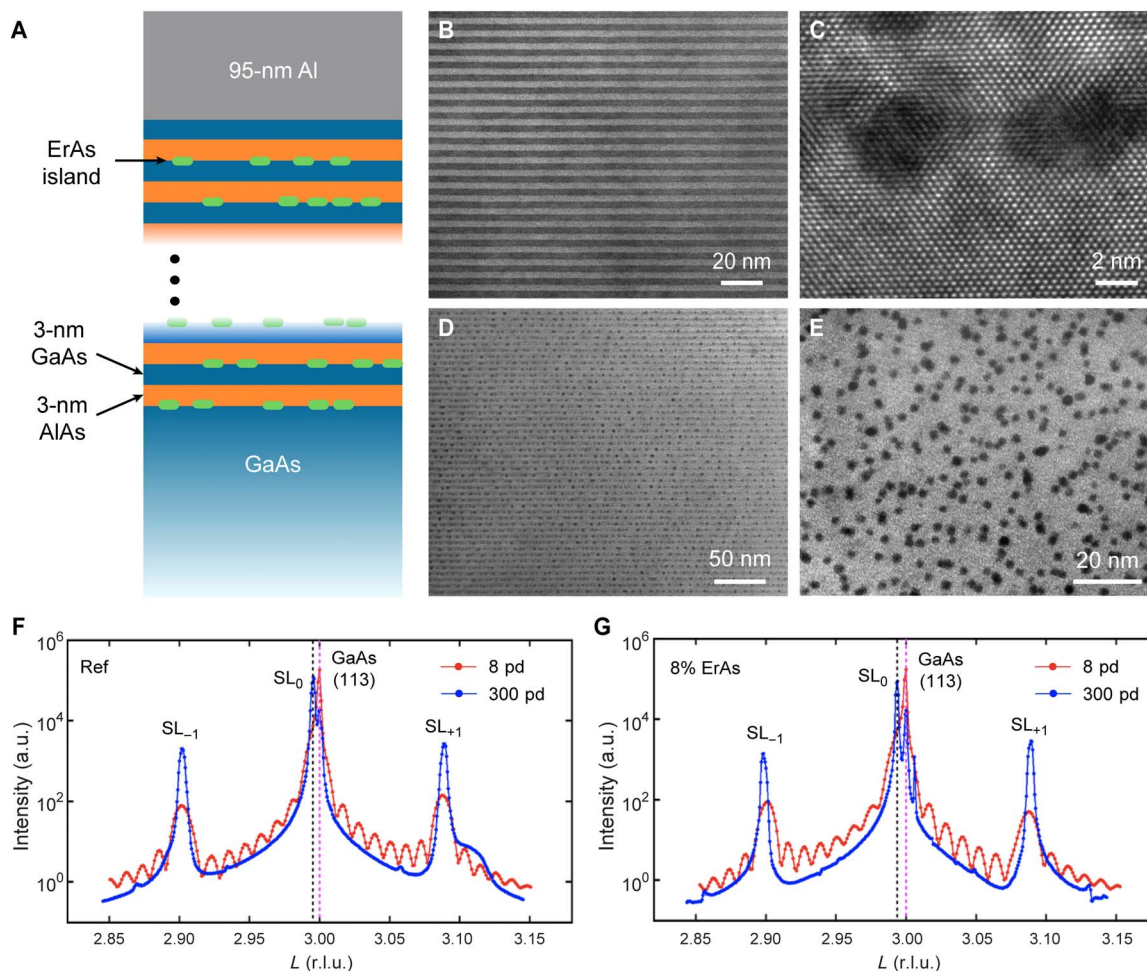||Corresponding author. Email: gchen2@mit.edu

Fig. 1. GaAs/AlAs SLs with ErAs nanodots at the interfaces. (**A**) Schematic of the SL samples. All samples have the same period thickness of 6 nm (3 nm of GaAs and 3 nm of AlAs), while the numbers of periods vary. Three sample sets are distinguished by a varying density of ErAs dots at the GaAs-AlAs interfaces: (i) reference set with no ErAs, (ii) 8% areal coverage with dots, and (iii) 25% areal coverage. (**B**) Cross-sectional TEM of a reference SL. (**C**) High-resolution TEM (HRTEM) of the ErAs dots. (**D**) Cross-sectional and (**E**) plan-view TEM of a sample with 8% ErAs coverage. (**F**) The 0th-order SL Bragg peak in reciprocal lattice unit (r.l.u.) along the sample growth direction, which indicates the average lattice spacing of an SL period and thereby the average lattice strain level in the SLs, where the average strain level difference between an 8- and a 300-period (pd) reference sample is determined to be $\sim$4.5 $\times$ 10^{-5}, while for samples with 8% ErAs coverage in (**G**), the strain level difference remains as low as 1.5 $\times$ 10^{-4}. a.u., arbitrary units.

the quality and consistency of the SLs throughout the sample thickness and the random distribution of the nanodots at the interfaces. The 25% ErAs interface coverage leads to a slight variation in the layer planarity that propagates through the SLs, as manifested by slight thickness variations at the surface (fig. S2, D to F), while the SLs with 8% ErAs coverage do not show a discernible variation from the bottom to the top of even the thickest samples (fig. S2, A to C). To quantify disorder and strain in the SLs, we performed a series of synchrotron x-ray diffraction (XRD) measurements. Comparing the 8- and 300-period SLs, the XRD shows a difference in the average strain level of only $\sim$4.5 $\times$ 10^{-5} for the reference samples (Fig. 1F), and even with 8% ErAs coverage, the strain level difference remains as low as 1.5 $\times$ 10^{-4} (Fig. 1G). Furthermore, by using grazing incidence, we compared the strain level at the top of the 300-period SLs to the average strain over the entire SLs and obtained a difference of 3.6 $\times$ 10^{-4} (2.1 $\times$ 10^{-4}) for the reference (8% ErAs) samples (fig. S3, A and B), indicating good growth uniformity even in the thickest samples. The presence of long-range disorder is further excluded through TEM-based strain mapping, which shows similar strain levels at the top and bottom of the SLs (fig. S3, C to E). In addition, polarized

neutron reflectometry (PNR) (fig. S3F) measured a period thickness of 6.14 nm in the SLs with 8% ErAs and 6.2 nm in those with 25% ErAs, consistent with the TEM observations. Together, these characterizations demonstrate that the potential effect of long-range disorder and strain on the measured thermal transport results can be ruled out.

The thermal conductivities of the SLs as a function of temperature, measured with time-domain thermoreflectance (TDTR) (13), are shown in Fig. 2 (representative data and sensitivity analyses are provided in figs. S4 to S7 and S12). For all the SLs, the thermal conductivity rapidly increases with increasing temperature up to about 100 K, above which the thermal conductivity roughly plateaus (Fig. 2, A to F). The addition of ErAs nanodots decreases the overall SL thermal conductivity, with a greater areal coverage leading to a greater decrease in thermal conductivity (Fig. 2, A to C). For small numbers of periods, the thermal conductivity also increases with increasing number of periods, indicating the presence of coherent phonon thermal transport (Fig. 2, G to I, and fig. S8) (13). The interface roughness and atomic mixing primarily scatter high-frequency phonons. The embedded ErAs dots have the additional effect of scattering phonons over a wide frequency range (elaborated later via modeling),
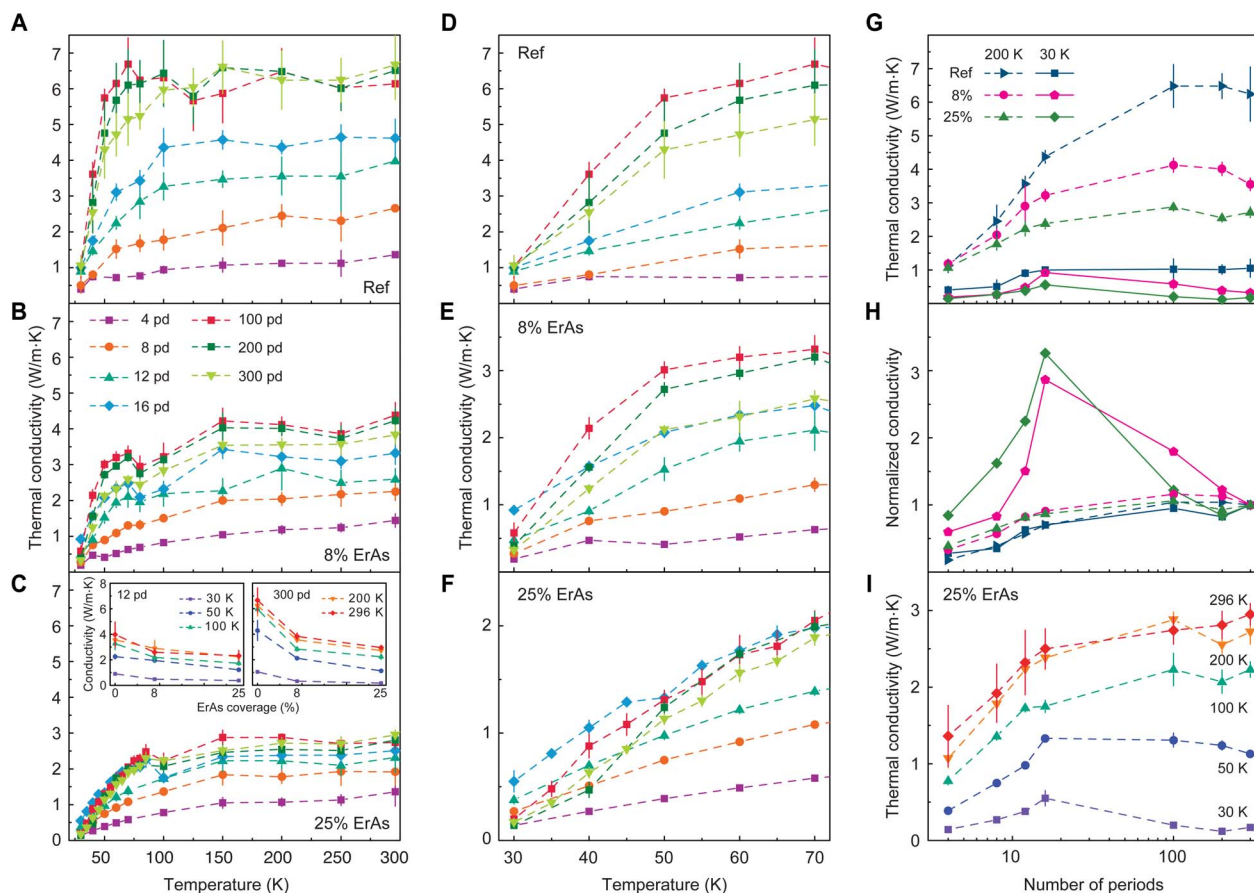
Fig. 2. Measured thermal conductivity of the SLs. Thermal conductivity as a function of temperature from 30 to 296 K for the three sets of samples. (**A**) Reference samples with no ErAs at the interfaces. (**B**) Samples with 8% of the GaAs-AlAs interfaces covered by ErAs nanodots. (**C**) Samples with 25% ErAs interface coverage. (**D** to **F**) Magnify the same data in (A) to (C) in the 30 to 70 K range. (**G** to **I**) Dependence of thermal conductivity on the number of periods. (**G**) At 200 K, the thermal conductivity first increases with increasing number of periods and then saturates, suggesting that some phonons traverse the SLs coherently. At 30 K, the thermal conductivity behaves similarly in the reference sample, but in the samples with ErAs dots, the thermal conductivity decreases after reaching a peak at a small number of periods. (**H**) When the thermal conductivities of all samples in (G) are normalized to that of the 300-period samples, the anomalous low-temperature trend for samples with ErAs dots is even more pronounced. (**I**) As the temperature increases, the thermal conductivity of the samples with 25% ErAs dots begins to match the trend seen in the reference samples, a uniform increase of thermal conductivity with increasing number of periods. Error bars represent 1 SD.

decreasing the range of coherent phonons that propagate through the en-tire SL without undergoing scattering. As more dots are added, the affected range grows. This is indicated by the decreasing thermal conduc-tivity with increasing ErAs density and also, notably, by the greater overall decrease in thermal conductivity for the samples with more SL periods (insets of Fig. 2C), as compared with those with a small number of periods. This latter observation bolsters our previous work on coherent phonon heat conduction in SLs (*13*). By adding scatterers at the SL inter-faces, we are able to reduce the role of coherent phonon transport in SLs and decrease the SL bulk thermal conductivity by a factor of two. We should also mention that the use of nanodots to increase the scattering of intermediate-wavelength phonons has been studied before both theoretically and experimentally (*19–22*). In particular, Pernot *et al.* (*22*) compared the measured thermal conductivities of Ge dots–based Si/Ge SLs to the simulated thermal conductivities of Si/Ge SLs with perfect interfaces and no dots. This comparison suggested that the Ge dots–based SLs can have five times lower thermal conductivity than SLs without nanodots. The major differences between our study and previous studies (*22*) are that (i) GaAs/AlAs SLs with and without ErAs dots have identical crystal structures, allowing for a direct com-

parison between simulation and experimental data, and (ii) whereas previous studies focused on thermally thick SLs with different period thicknesses, we fixed the period thickness of the SLs while varying the total number of periods. Our approach allows us to discover unique wave effects as we discuss below.

The dependence of thermal conductivity on the total thickness of the SLs reveals a very interesting trend (Fig. 2, D to I). At temperatures above 100 K, the samples with a small number of periods (4, 8, 12, and 16) consistently show an increasing thermal conductivity with increasing number of periods (Fig. 2, G and I), which signifies that transport is primarily ballistic. As the number of periods increases, the thermal conductivities of the SLs eventually saturate to values that are much lower than either bulk parent material (45 W/m·K for GaAs and 90 W/m·K for AlAs at room temperature) (*23*), and the saturation values are even lower than that of the corresponding bulk homogenous alloys (~10 W/m·K) (*23*). Extensive past modeling and experimental studies on the thermal conductivity of SLs, together with recent first principles simulations, can explain these observations well. The lower-than-bulk effective thermal conductivity is mainly due to the scattering of short-wavelength phonons by the internal interface roughness of the

SLs. However, long-wavelength phonons are not effectively scattered by this interface roughness. They traverse the thin (small number of periods) SLs ballistically while maintaining their phase, leading to an increasing thermal conductivity with an increasing number of periods. With a sufficiently large number of periods, these coherent, long-wavelength phonons are eventually scattered by inelastic phonon-phonon processes. Thus, on a coarse-grained level and in the large number of periods limit, both long- and short-wavelength phonons can be viewed as undergoing diffusive transport, even though high-frequency phonons are dominantly scattered at individual interfaces and long-wavelength phonons are scattered via phonon-phonon processes after traversing many interfaces, leading to the experimentally observed saturation of thermal conductivity with increasing number of periods.

At lower temperatures, however, SLs with ErAs nanodots at the interfaces show a different and unexpected trend. The thick (large number of periods) SLs with ErAs dots have stronger temperature dependence than the thin SLs, leading to a crossover of thermal conductivity (Fig. 2, E and F). Below 60 K, the SLs with 25% ErAs coverage at the GaAs-AlAs interfaces and fewer periods (12 and 16) have a higher thermal conductivity than the thickest SLs. This transition also happens in the samples with 8% ErAs coverage but is absent from the reference samples (Fig. 2D). To highlight the transition, we plotted the measured thermal conductivity as a function of number of periods and compared between reference samples and SL with ErAs dots at 30 and 200 K (Fig. 2G). We normalize the thermal conductivities of all samples to those of the corresponding 300-period SLs (Fig. 2H) and observe a peak in both the 8 and 25% ErAs samples at 30 K. In Fig. 2I, we plot the changing behavior of the 25% ErAs SLs at different temperatures, which shows that the peak also exists at 50 K but disappears at higher temperatures.

The observation of the peaks in samples at low temperatures with two different concentrations of ErAs nanodots at the interfaces suggests that, rather than being caused by small variations in the arrangement of the dots across different samples, a new heat conduction mechanism, which reduces the transport of long-wavelength, low-frequency (terahertz range) phonons, is unfolding with an increasing sample thickness. This unexpected trend strongly points to the presence of phonon localization in these SLs. Localization effects in phonon transport are expected to unfold over an increasing sample thickness, as certain phonon modes make the transition from being propagating to nonpropagating due to destructive interference from multiple elastic scattering events (24). Localization is characterized by a phonon frequency–dependent localization length, ξ. Phonon transmission decays exponentially for localized modes as $e^{-L/\xi}$, where L is the total thickness of the SL. When L is much smaller compared with ξ, phonon transport is in the ballistic regime, and the thermal conductivity increases with the total thickness. As the total thickness of the SLs increases, some phonons become localized and do not contribute to heat conduction anymore, leading to a decreasing thermal conductivity with increasing thickness. This transition from ballistic to localized transport is evidenced by the presence of a maximum in the measured thermal conductivity, as shown in Fig. 2 (G to I), and will be supported by simulations later.

We do not observe localization of heat conduction at room temperature because with increasing temperature, a broader range of phonon frequencies contributes to the thermal conductivity. Higher-frequency phonons experience diffuse interface scattering and phase-breaking phonon-phonon scattering, leading to a trend of saturating thermal conductivity with increasing number of periods (Fig. 2, G to I). This is correlated with the ballistic-to-diffusive transition typically observed in nanostructures. At lower temperatures, the phonon population shifts

more to lower-frequency phonons so phonon-phonon scattering becomes less effective, making the contributions from localized phonons observable. This ballistic-to-localized phonon transport behavior has never been observed before.

Simulations supporting localization

We carried out simulations to further explain the experimental observations (25). We used atomistic Green's function simulations to compute phonon transmission across SLs with (i) perfect interfaces, (ii) atomic mixing (roughness) at interfaces, and (iii) nanodots at each interface, following established methods with accelerated algorithms (see Materials and Methods) (13, 26). Because of computational limitations, we rescaled the lateral size of the system so that the cross-sectional area was 1.68 nm by 1.68 nm ($3a \times 3a$, where a is the lattice constant) with periodic boundary conditions in the lateral direction. The interface roughness comprises a random mixing of Ga and Al atoms in one crystal lattice on each side of the interfaces, and the nanodots are spheres with a diameter of two lattice constants, or 1.12 nm, with their centers positioned randomly at both the GaAs-AlAs and AlAs-GaAs interfaces. The force constants are taken to be the average between pure GaAs and AlAs, while ErAs is represented by a sphere of atoms with the same lattice structure but different mass (see Materials and Methods for details). The results presented in Fig. 3 represent the averages of an ensemble of 20 random distributions of nanodots. Figure 3A shows the calculated transmission functions for SLs with only atomic mixing–caused roughness at the interfaces and for SLs with both roughness and nanodots at the interfaces. As the number of periods increases, the transmission function decreases in both scenarios, but the decrease is much more drastic in the samples with both roughness and nanodots. The transmittance as a function of frequency for these cases further highlights this effect (Fig. 3B). At frequencies around 2 THz, there is a notable dip in the transmission functions with increasing numbers of periods in the SLs with roughness and nanodots. From these figures, we observe that phonon transmittance is significantly reduced in samples with nanodots for frequencies near the zone edges (near 1.5 THz), consistent with the established picture that it is easier to localize at band edges (a calculated dispersion relationship is shown in fig. S9) (18, 24). In Fig. 3C, we plot the transmission function versus the number of periods for normal incidence phonons with a frequency of 1.65 THz, which shows an exponential decay in the transmission of these phonons in the SLs with roughness and nanodots. Figure 3 (A and B) also shows that nanodots localize phonons over a wide frequency range.

We follow the formalism in MacKinnon and Kramer (27) to compute the localization lengths in the 300-period samples at different frequencies (Fig. 3D) in the SL structures with interface roughness and nanodots. The inelastic phonon MFPs due to phonon-phonon scattering obtained from first principles simulations (13) at 30 and 300 K are also shown in Fig. 3D. At 30 K, the inelastic MFP, on average, is much longer than the localization length so that phonons maintain their phases during transport and localization can occur. In Fig. 3E, we show the contributions of each phonon frequency to the overall thermal conductivity for the three 100-period samples in Fig. 3C with a thermal conductivity accumulation plot. The accumulated thermal conductivity of the SL with nanodots has a flat region between 1.5 and 2.8 THz. In this range, most phonons are localized and do not contribute to thermal conductivity. Using the transmission functions, we calculate the thermal conductivity as a function of number of periods (inset of Fig. 3F), neglecting the effects of anharmonic scattering that is much longer than the total SL thickness. Figure 3F shows the normalized (to the 300-period SLs) thermal conductivity (at 30 K) of SLs with interface roughness and SLs with both interface
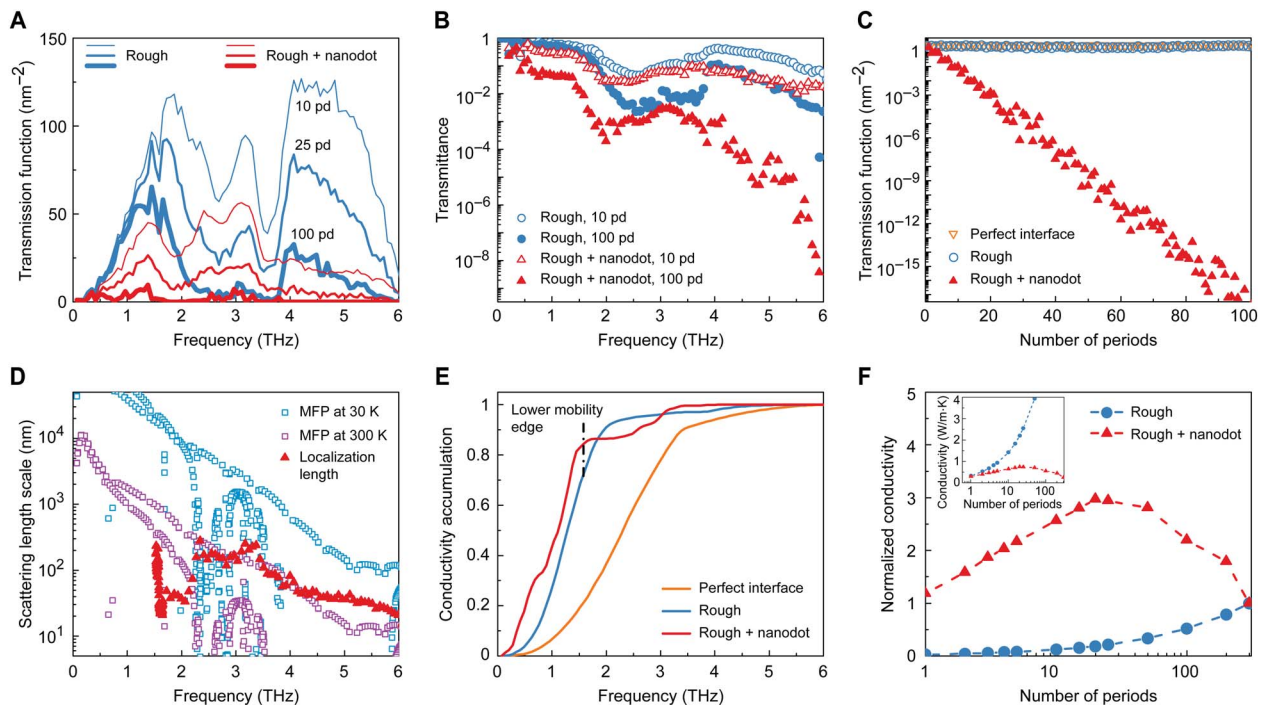
Fig. 3. Computed phonon transport properties of SLs with nanodots. (**A**) Frequency-dependent transmission functions summed over all angles versus number of periods. (**B**) Transmittances of phonons in SLs with only roughness and SLs with both roughness and nanodots. (**C**) Transmission functions for 1.65-THz phonons at normal incidence in SLs with perfect interfaces, rough interfaces, and both roughness and nanodots at the interfaces. (**D**) Inelastic MFPs of a perfect SL at 30 and 300 K and localization length in an SL with both roughness and nanodots at the interfaces. (**E**) Thermal conductivity accumulation for perfect SLs, SLs with rough interfaces, and SLs with both roughness and nanodots at the interfaces at 30 K. (**F**) Normalized thermal conductivity as a function of number of periods for rough SLs with and without ErAs nanodots at the interfaces at 30 K (inset shows thermal conductivity values).

roughness and nanodots. We note that the predicted thermal conductivity value and peak location are in the same range as those observed in the experiments (Fig. 2E), although we do not expect one-to-one comparison due to approximations made. The consistency of both the existence of the peak and its location in terms of the number of periods between the simulations and experiments further support our explanation that the experimental observation is due to phonon localization.

DISCUSSION
Anderson localization originates from interferences between multiple-wave scatterings in strongly disordered media (*18, 24, 28, 29*). Ever since Anderson's pioneering work on electron localization in a random potential (*29*), the localization of waves, in general, has been extensively studied. It has been found that in disordered one-dimensional (1D) and 2D media, all finite frequency phonons are localized, while in 3D, mobility edges separating low-frequency extended states and high-frequency localized states exist (*24, 30*). However, heat conduction is a broadband phenomenon, and no experiments have shown the impact of localization. In bulk dielectric and semiconductor crystals, where phonon transport dominates heat conduction, the wave vectors, k, at the band edges are high. In accordance with the modified Ioffe-Regel criterion for strong wave localization in three dimensions (*31*), $l \times k \leq 1$, localized phonons in a bulk material have MFPs, l, on the order of angstroms. Since phonons contributing to the thermal conductivity in bulk crystals have much longer MFPs, the Ioffe-Regel condition is difficult to meet, and observations of localization have been elusive. Furthermore, not all phonons satisfying the Ioffe-Regel criterion are localized (*32*). A minimum in the thermal

conductivities of some SLs was used by Venkatasubramanian (*33*) as a sign of localization, but later works showed that these minima were the result of the competition between coherent and incoherent transport in SLs (*14, 34*). The plateaus in the thermal conductivities of glasses and aggregates at low temperatures were thought of as the combined effects of localization and diffusion, although simulations show that localization was not dominant (*35*). In these materials, however, the phonon MFPs are on the order of tens of angstroms, much shorter than in typical crystalline materials. Computational studies of thermal transport in boron nitride with isotopic impurities, where the mass mismatch was small, found that localization is unobservable in thermal transport properties (*36*). A few publications have shown traces of phonon localization in thermal transport simulations, including molecular dynamics simulations in SLs with randomized period thicknesses (*12*) and continuum mechanics–based simulations of cross section–modulated core-shell nanowire SLs (*11*). These simulations more closely model low-dimensional structures, for which localization is easier to observe.

We can observe the consequences of phonon localization on heat conduction through the GaAs/AlAs SLs with ErAs nanodots because of several factors. First, natural interface mixing in GaAs/AlAs SLs scatters high-frequency phonons and reduces their contribution to thermal conductivity (Fig. 3, A and B). Figure 3E shows that with interface mixing, phonons contributing to heat conduction are limited to a narrow band of frequencies from 0.5 to 1.7 THz. Second, zone folding in SLs reduces the wave vector at the Brillouin zone boundary by approximately an order of magnitude, from the lattice constant of bulk crystals (~5 Å) to the 6-nm lattice constant of the SL. The reduced wave vector allows longer MFP phonons to satisfy the modified Ioffe-Regel

criterion. The calculated localization length in the 300-period SLs with nanodots diverges at 1.58 THz (Fig. 3D), which we identify as the lower mobility edge. The larger dot size in our samples will further push the mobility edge to an even lower frequency that overlaps more with phonons contributing to heat conduction. Furthermore, Fig. 3D also shows that the localization length jumps around 2.3 THz. This window of short localization lengths is consistent with the theoretical prediction by Kirkpatrick (30) on acoustic waves and John (18) on photon localization in SLs with lateral disorder. Even above the second mobility edge at 2.3 THz, however, our simulated localization length is still shorter than the inelastic scattering length, suggesting that localization is still possible even at higher frequencies. Third, the diameter of the ErAs is approximately 3 nm, and on average, their spacing is 9 nm for the SLs with 8% coverage and 5 nm for those with 25% areal coverage. These are comparable to the phonon wavelengths at the boundaries of the folded zone, increasing the multiple scatterings of these phonons and leading to their localization.

At higher temperatures, some low-frequency phonons can still be localized despite the absence of a localization signal in the measured thermal conductivity, as suggested by Fig. 3D, since these phonons have inelastic MFPs longer than the localization length. We conducted a Raman scattering experiment to probe the first few bands of the folded band structure in the SLs. The measured phonon spectra of the first two bands of selected SLs at room temperature are shown in fig. S10. The Raman experiment measures transverse phonons at the zone center rather than at the band edge (37). While the reference SLs show clear peaks at 0.75, 0.90, 1.65, and 1.80 THz, the ErAs-covered SLs do not display strong signals at the latter two bands. For 25% ErAs coverage, the first band disappears in the 300-period SL. We interpret the disappearing bands as a result of wave cancellation that leads to localization but emphasize that there is currently no clear understanding on what a Raman signal should look like due to phonon localization. We also measured the pump modulation frequency dependence (38, 39) on the measured thermal conductivities of the SLs, and the experimental results show much weaker frequency dependence in samples with ErAs dots (fig. S11, with further discussion in the Supplementary Materials).

In summary, we have demonstrated the potential of engineering phonon waves to reduce the thermal conductivity in SLs. By using ErAs nanodots, we reduce the thermal conductivity of thick SLs by as much as a factor of two compared with the samples without dots. At low temperatures, we observed experimentally that the thermal conductivity of these SLs first increases and then decreases with increasing number of periods, consistent with the phonon localization effect. Our Green's function–based simulations further confirm this ballistic-to-localized transport transition. At higher temperatures, the thermal conductivity versus the number of SL periods follows the ballistic-to-diffusion transition behavior. These observations open up new opportunities to engineer phonon thermal conductivity via wave effects.

MATERIALS AND METHODS
Sample preparation
GaAs/AlAs SLs with ErAs nanoparticles were grown epitaxially (40). All the samples were grown in a Veeco Gen III MBE (Molecular Beam Epitaxy) system. Solid source materials Ga, Al, Er, and a Veeco valved cracker for As were used for the growths. Sub–monolayer (ML) ErAs deposition was inserted at the GaAs-AlAs interfaces; we aimed for surface coverage of 8 and 25% by 0.32-ML and 1-ML

ErAs deposition, respectively. Depositions of ErAs were described in MLs as if the ErAs had grown in a layer-by-layer growth mode (1 ML of ErAs = 2.87 Å of film thickness). Nanodots were formed because of self-assembly of the deposited atoms. The growth rates of GaAs and AlAs were set to be around 1 μm/hour, while the ErAs growth rate was kept at 0.02 ML/s. The As_2 overpressure was maintained at 1.07×10^{-3} Pa during the growth. All the samples were finished with a 3-nm GaAs layer to prevent possible oxidation of either AlAs or ErAs. ErAs has a lattice constant of 5.74 Å, while that of GaAs is 5.6533 Å, a lattice constant mismatch of 1.53%. In general, we believe the growth rate calibration of ErAs can have a variation of a few percent. We estimated the surface coverage by dividing the ErAs layer thickness (from the growth rate calibration) by 4 MLs (which was observed from previous TEM studies showing that most of the ErAs dots tend to form 4 MLs tall). TEM images of the different sample configurations are shown in Fig. 1 and figs. S1 and S2.

Synchrotron-based XRD
A series of GaAs/AlAs SLs were characterized by synchrotron XRD at 12-ID-D of Advanced Photon Source at Argonne, including 8- and 300-period samples with and without ErAs dots. The x-ray monochromator energy resolution $\Delta E/E$ is about 1×10^{-4}, while the XRD angular resolution $\Delta\theta/\theta$ is about 1.5×10^{-4}. With this level of resolution, relative shifts of the Bragg peak on the order of 10^{-5} can be detected. In the measurement, the 0th-order SL Bragg peak was used to quantify the average lattice spacing of SL periods in the system, therefore signifying the average vertical strain level of the system. To enhance the sensitivity to detect any strain level variations, we measured at around (113) asymmetry Bragg peak of GaAs. In addition, to resolve the depth-dependent strain level distribution of the thick 300-period SLs (reference and with ErAs dots), we adopted different angles of incidence of the x-ray beams, from penetrating the bulk SLs to limiting the signal sensitivity only to the top layers of the SLs.

TEM-based strain mapping
The cross-sectional TEM samples for strain mapping studies were prepared using the focused ion beam technique with additional ion milling process. To realize high-resolution TEM-based strain mapping, the 300-period SLs were thinned both bottom-to-top and top-to-bottom to make the bottom region and the top region comparable. HRTEM images were acquired using the high-angle annular dark-field detector on a double aberration correction JEOL ARM-200CF at Brookhaven National Laboratory. The strain maps were retrieved using geometric phase analysis from HRTEM images by selecting substrate areas as a reference (41, 42).

Polarized neutron reflectometry
The structure and composition of the 8-period SL samples were characterized by PNR, performed at the Polarized Beam Reflectometer beamline at the National Institute of Standards and Technology (NIST) Center for Neutron Research, with an in-plane guide field $\mu_0 H = 0.7$ T and at $T = 4$ K (fig. S3). Compared with the 8% ErAs sample, the 25% ErAs sample showed a shallower dip, indicating an increase in interface roughness upon the addition of the ErAs nanodots. The higher-frequency oscillations observed for the 25% ErAs SL indicate a slight increase in the lattice period, which is quite reasonable since the lattice constant of ErAs exceeds that of GaAs by 1.53%. To understand the detailed structure and further information about the concentration of ErAs at the interfaces, we refined the PNR curves using a differential

evolution algorithm by GenX (43), where the structure, roughness, and ErAs concentration were extracted. The results are consistent with those observed with TEM analysis.

Time-domain thermoreflectance

Briefly, a high-power (~50 to 100 mW) laser pulse impinged on a metal optothermal transducer layer coated on the sample. This laser pulse excited surface electrons that quickly thermalized, sending a heat pulse propagating through the metal and then through the sample, away from the surface. A time-delayed probe pulse measured the changing surface reflectivity caused by changing temperature. A multidimensional, multilayer heat equation was fit to the resulting cooling curve, yielding the thermal conductivity of the SL layers (13). The system used here is described in further detail in a previous publication (44). We deposited a 100-nm-thick Al optothermal transducer layer on the SLs and a calibration sapphire substrate. We confirmed the thickness of the Al transducer layer by matching the TDTR-measured thermal conductivity value of the sapphire substrate with the known literature value. Low-temperature measurements were conducted by mounting the samples in a high-vacuum (~10^{-3} Pa) cryostat. The transient reflectance of the sample surface was measured with a Si photodiode.

Each sample was probed at around three to five different locations. At each location, the samples were measured under four different pump modulation frequencies—3, 6, 9, and 12 MHz—with three individual data traces collected for each modulation frequency. The three runs at each frequency were averaged, and the Fourier fitting analysis was performed on the resultant average curve at each modulation frequency for each location. Sample sets of fitting curves for the reference samples and the 25% ErAs coverage samples for different SL thicknesses and at different temperatures are shown in figs. S4 and S5.

The data were fit to a four-layer model comprising the metal optothermal transducer, the interface between the metal and the SL, the SL, and a semi-infinite substrate. The data were fit for the interface conductance between the metal and the SL, and the SL thermal conductivity. The other required parameters for the fitting were taken from the literature. Since the volumetric fraction of ErAs was small compared with GaAs and AlAs (0.32 and 1 ML of ErAs per 10 MLs of GaAs or AlAs for the 8 and 25% nanodot areal coverage samples, respectively), the heat capacity was taken to be the average of GaAs and AlAs. An initial guess for the interface conductance between the SL, capped by a 3-nm GaAs layer, and the Al optothermal transducer layer were taken from previous measurements of the interface conductance between a bulk GaAs substrate and an Al layer deposited with an identical procedure. Due to its size dependence, the effective thermal conductivity of GaAs at low temperatures was also taken from previous measurements.

SL phonon dispersion and anharmonic scattering

The phonon dispersion and anharmonic phonon-phonon scattering rates can be derived on the basis of the harmonic and anharmonic interatomic force constants (IFCs). We first fit the IFCs for pure GaAs and AlAs, respectively, based on the first principles data regarding forces acting on different atoms and their displacements in a large supercell ($2 \times 2 \times 2$ conventional unit cells, 64 atoms), with imposed translational and rotational invariances. Harmonic IFCs up to the fifth nearest neighbor and third-order anharmonic IFCs up to the first nearest neighbor were considered. The force-displacement data were computed using the density functional theory as implemented in the QUANTUM ESPRESSO package (45), for which we used the norm-conserving pseudopoten-

tial with the Perdew and Zunger (46) local density approximation for the exchange-correlation functional, a cutoff energy of 60 rydberg, and a $16 \times 16 \times 16$ **k**-mesh. We then took the average of the IFCs (both harmonic and anharmonic) corresponding to pure GaAs and AlAs as the IFCs for the SL, which is a good approximation due to the small lattice mismatch between GaAs and AlAs and has previously been used for calculating the thermal conductivity of SLs (13). For further calculating the phonon dynamics, the unit cell lattice constant for the GaAs/AlAs SL was taken to be the average (5.5722 Å) of the calculated values in pure GaAs and AlAs.

The phonon dispersion can be computed from the dynamical matrix, whose matrix elements, in real space, take the form $D_{ij} = \frac{\phi_{ij}}{\sqrt{m_i m_j}}$, where ϕ_{ij} represents the harmonic IFC that couples the ith and jth atoms of mass m_i and m_j, respectively. Although this model did not describe the local strain effects from either the interfaces or the ErAs nanodots, the dispersion of the phonon frequency for an SL with a period of 5.57 nm (fig. S9) agreed well with the previously calculated dispersion for a 24-nm period GaAs/AlAs SL using semiempirical force constants in the work of Luckyanova et al. (13)

The phonon MFP due to anharmonic phonon-phonon scattering was calculated by $\Lambda_{q\lambda} = v_{q\lambda}\tau_{q\lambda}$, where $v_{q\lambda}$ is the phonon group velocity and $\tau_{q\lambda}$ is the phonon relaxation time. The group velocity was obtained from the phonon dispersion, while the relaxation times were calculated using the lowest-order three-phonon scattering process via (47, 48)

$$\frac{1}{\tau_{\mathbf{q}\lambda}^{ph-ph}} = \frac{1}{2h^2 N_{\mathbf{q}}} \cdot \sum_{q_1\lambda_1, q_2\lambda_2} \left| V_{\mathbf{q}\lambda, \mathbf{q}_1\lambda_1, \mathbf{q}_2\lambda_2} \right|^2$$

$$\left\{ \begin{array}{l} (n^0_{\mathbf{q}_1\lambda_1} + n^0_{\mathbf{q}_2\lambda_2} + 1) \cdot \left[\begin{array}{l} \delta(\omega_{\mathbf{q}_1\lambda_1} + \omega_{\mathbf{q}_2\lambda_2} - \omega_{\mathbf{q}\lambda})\delta_{\mathbf{q}+\mathbf{q}_1+\mathbf{q}_2, \mathbf{G}} \\ -\delta(\omega_{\mathbf{q}_1\lambda_1} + \omega_{\mathbf{q}_2\lambda_2} + \omega_{\mathbf{q}\lambda})\delta_{\mathbf{q}+\mathbf{q}_1+\mathbf{q}_2, \mathbf{G}} \end{array} \right] \\ + (n^0_{\mathbf{q}_2\lambda_2} - n^0_{\mathbf{q}_1\lambda_1}) \cdot \left[\begin{array}{l} \delta(\omega_{\mathbf{q}_1\lambda_1} - \omega_{\mathbf{q}_2\lambda_2} - \omega_{\mathbf{q}\lambda})\delta_{\mathbf{q}+\mathbf{q}_1+\mathbf{q}_2, \mathbf{G}} \\ -\delta(\omega_{\mathbf{q}_1\lambda_1} - \omega_{\mathbf{q}_2\lambda_2} + \omega_{\mathbf{q}\lambda})\delta_{\mathbf{q}+\mathbf{q}_1+\mathbf{q}_2, \mathbf{G}} \end{array} \right] \end{array} \right\}$$

(1)

where $V_{q,\lambda,q_1,\lambda_1,q_2,\lambda_2}$ are the three-phonon coupling matrix elements and depend on the third-order IFCs (47). For the MFP calculation, due to the computational complexity, we chose the SL structure to have three conventional cells for each layer (GaAs or AlAs) perpendicular to the SL interface (dimensions: 5.5722 Å by 5.5722 Å by 33.43 Å). A $16 \times 16 \times 3$ **q**-mesh was used for calculating the phonon relaxation times (Eq. 1), and the convergence with respect to the mesh was checked. We also checked the phonon relaxation times of the SL with smaller period (dimensions: 5.5722 Å by 5.5722 Å by 22.29 Å) and found that the phonon MFPs have small differences. Therefore, our calculated results should be close to the experimental configuration, which has a slightly larger period.

Green's function simulation

The atomistic Green's function (25, 26) approach models the heat transfer through a finite-size device that is coupled to semi-infinite reservoirs on each end. The dynamical matrix of the entire system can be written as

$$H = \begin{bmatrix} H_{\mathrm{L}} & \tau_{\mathrm{LD}} & 0 \\ \tau_{\mathrm{LD}}^\dagger & H_{\mathrm{D}} & \tau_{\mathrm{DR}} \\ 0 & \tau_{\mathrm{DR}}^\dagger & H_{\mathrm{R}} \end{bmatrix} \quad (2)$$

where H_L, H_R, and H_D are the dynamical matrices of the left reservoir, right reservoir, and device region, respectively. τ_{LD} is the dynamical matrix that couples the left reservoir to the device, and τ_{DR} is the dynamical matrix that couples the device to the right reservoir. This formalism is only valid when the reservoirs are uncoupled from one another. For semi-infinite reservoirs, the dynamical matrix of Eq. 2 is infinitely large. To make this problem tractable, the interactions between the device and the reservoirs were encoded in self-energy terms $\Sigma_L = \tau_{LD}^\dagger g_L \tau_{LD}$ and $\Sigma_R = \tau_{RD}^\dagger g_R \tau_{RD}$ where $g_{L,R}$ are the surface Green's functions obtained from a real space decimation method (49). The Green's function of the device region were computed as $G_D = (\omega^2 - H_D - \Sigma_L - \Sigma_R)^{-1}$, where ω^2 is the square of the phonon eigenfrequency. Defining $\Gamma_{L,R} = i(\Sigma_{L,R} - \Sigma_{L,R}^\dagger)$, the transmission function for a given frequency ω and transverse wave vector k can be written as

$$\Xi(\omega,k) = Tr[\Gamma_L G_D \Gamma_R G_D^\dagger] \quad (3)$$

noting that the frequency and wave vector arguments on the right-hand side are implicit, and the results presented in Fig. 3 include all wave vectors except Fig. 3C. Defining $\Xi(\omega) = \frac{1}{N_k}\sum_k \Xi(\omega,k)$ as the normalized sum over N_k points in the Brillouin zone, the thermal conductance at a given temperature T can be expressed as

$$K(T) = \frac{1}{2\pi A_D}\int_0^\infty \hbar\omega \frac{\partial f(\omega,T)}{\partial T}\Xi(\omega)d\omega \quad (4)$$

where A_D is the area of the device's cross section and $f(\omega, T)$ is the Bose-Einstein distribution function.

The computation of Eq. 4 only requires the subspace of Green's function matrix elements that connect the right reservoir and the left reservoir. We denoted the set of matrix elements of this subspace as G_{1N}. G_{1N} was recursively computed from the Dyson's equation. Since G_{1N} corresponds to the probability amplitude for a phonon to propagate across the entire device, the localization length l_{loc} can be determined from (27)

$$\frac{1}{l_{loc}} = -\lim_{N\to\infty}\frac{\ln(Tr[|G_{1N}|^2])}{2Nl} \quad (5)$$

for a system of N periods of length l. Because of computational limitations, localization lengths were extracted from an average of 10 configurations of 300-period (~1700 nm) devices, which also correspond to the thickest samples measured.

Modeling the randomness
Since the atomistic Green's function method models harmonic systems, scattering comes from the breaking of translational symmetry. In this particular case, the suppression of phonon transport is due to the presence of interfacial roughness and ErAs nanoparticles. Within one unit cell on each side of the interface, coordinates corresponding to the Ga/Al sublattice were chosen at random. In the case of interface roughness, the Ga or Al atom was replaced with Al or Ga, respectively. In the case of randomly placed ErAs nanodots, the coordinate corresponds to the center of the dot; consequently, all Ga and Al atoms within 0.5 nm of this point were replaced with Er atoms. In all these replacements, only mass was changed, while force constants were maintained the same.

ErAs grows in the rock salt structure instead of the zinc-blende structure of GaAs. Our approximation assumes that the mass difference is the major mechanism of phonon scattering, which is reasonable considering that Er is 6.29 and 2.40 times heavier than Al and Ga, respectively. Since the randomness introduces variance in the calculated thermal conductivity, a configurational average is necessary. The number of configurations, for a given sample thickness, is inversely proportional to its sample thickness to ensure constant computational cost for each data point in Fig. 3 (E and F). For our data, one configuration was used for the 100-period device regions, four configurations were used for the 25-period device region, and 100 configurations were used for the 1-period device region, etc.

Raman scattering experimental configuration
Raman spectra for several samples are shown in fig. S10. The low-frequency (<100 cm^{-1}) Raman spectra were obtained with a Horiba Jobin-Yvon T64000 triple-grating Raman spectrometer under a $Z(XX)\bar{Z}$ backscattering configuration. The excitation laser was a frequency-doubled Nd:YAG laser with a wavelength of 532.1 nm, and the power incident on the sample was 7.2 mW. The acquisition time was 60 s to ensure a sufficient signal-to-noise ratio. A 100× objective lens with a numerical aperture (NA) of 0.95, a motorized XYZ stage, and three 1800 grooves/mm grating were used. Both Stokes and anti-Stokes Raman lines were collected and were used to improve the measurements of Raman shifts. In contrast to the low-frequency measurement, high-frequency (>100 cm^{-1}) spectra were measured with a Horiba Jobin-Yvon HR800 Raman spectrometer using an objective lens with an NA of 0.90, an incident excitation laser power on the sample of 1.2 mW, and a shorter accumulation time of 15 s. The other measurement configurations were the same.

REFERENCES AND NOTES
1. D. G. Cahill, P. V. Braun, G. Chen, D. R. Clarke, S. Fan, K. E. Goodson, P. Keblinski, W. P. King, G. D. Mahan, A. Majumdar, H. J. Maris, S. R. Phillpot, E. Pop, L. Shi, Nanoscale thermal transport. II. 2003–2012. Appl. Phys. Rev. 1, 011305 (2014).
2. B. Poudel, Q. Hao, Y. Ma, Y. Lan, A. Minnich, B. Yu, X. Yan, D. Wang, A. Muto, D. Vashaee, X. Chen, J. Liu, M. S. Dresselhaus, G. Chen, Z. Ren, High-thermoelectric performance of nanostructured bismuth antimony telluride bulk alloys. Science 320, 634–638 (2008).
3. R. Venkatasubramanian, E. Siivola, T. Colpitts, B. O'Quinn, Thin-film thermoelectric devices with high room-temperature figures of merit. Nature 413, 597–602 (2001).

4. T. C. Harman, P. J. Taylor, M. P. Walsh, B. E. LaForge, Quantum dot superlattice thermoelectric materials and devices. *Science* **297**, 2229–2232 (2002).

5. A. I. Hochbaum, R. Chen, R. D. Delgado, W. Liang, E. C. Garnett, M. Najarian, A. Majumdar, P. Yang, Enhanced thermoelectric performance of rough silicon nanowires. *Nature* **451**, 163–167 (2008).

6. A. I. Boukai, Y. Bunimovich, J. Tahir-Kheli, J.-K. Yu, W. A. Goddard III, J. R. Heath, Silicon nanowires as efficient thermoelectric materials. *Nature* **451**, 168–171 (2008).

7. V. Narayanaamurti, Phonon optics and phonon propagation in semiconductors. *Science* **213**, 717–723 (1981).

8. M. Maldovan, Phonon wave interference and thermal bandgap materials. *Nat. Mater.* **14**, 667–674 (2015).

9. J.-K. Yu, S. Mitrovic, D. Tham, J. Varghese, J. R. Heath, Reduction of thermal conductivity in phononic nanomesh structures. *Nat. Nanotechnol.* **5**, 718–721 (2010).

10. C. W. Chang, D. Okawa, A. Majumdar, A. Zettl, Solid-state thermal rectifier. *Science* **314**, 1121–1124 (2006).

11. D. L. Nika, A. I. Cocemasov, D. V. Crismari, A. A. Balandin, Thermal conductivity inhibition in phonon engineered core-shell cross-section modulated Si/Ge nanowires. *Appl. Phys. Lett.* **102**, 213109 (2013).

12. Y. Wang, H. Huang, X. Ruan, Decomposition of coherent and incoherent phonon conduction in superlattices and random multilayers. *Phys. Rev. B* **90**, 165406 (2014).

13. M. N. Luckyanova, J. Garg, K. Esfarjani, A. Jandl, M. T. Bulsara, A. J. Schmidt, A. J. Minnich, S. Chen, M. S. Dresselhaus, Z. Ren, E. A. Fitzgerald, G. Chen, Coherent phonon heat conduction in superlattices. *Science* **338**, 936–939 (2012).

14. J. Ravichandran, A. K. Yadav, R. Cheaito, P. B. Rossen, A. Soukiassian, S. J. Suresha, J. C. Duda, B. M. Foley, C.-H. Lee, Y. Zhu, A. W. Lichtenberger, J. E. Moore, D. A. Muller, D. G. Schlom, P. E. Hopkins, A. Majumdar, R. Ramesh, M. A. Zurbuchen, Crossover from incoherent to coherent phonon scattering in epitaxial oxide superlattices. *Nat. Mater.* **13**, 168–172 (2014).

15. G. Chen, Thermal conductivity and ballistic-phonon transport in the cross-plane direction of superlattices. *Phys. Rev. B* **57**, 14958–14973 (1998).

16. S.-i. Tamura, Y. Tanaka, H. J. Maris, Phonon group velocity and thermal conduction in superlattices. *Phys. Rev. B* **60**, 2627–2630 (1999).

17. S. C. Huberman, J. M. Larkin, A. J. H. McGaughey, C. H. Amon, Disruption of superlattice phonons by interfacial mixing. *Phys. Rev. B* **88**, 155311 (2013).

18. S. John, Strong localization of photons in certain disordered dielectric superlattices. *Phys. Rev. Lett.* **58**, 2486–2489 (1987).

19. P. Chen, N. A. Katcho, J. P. Feser, W. Li, M. Glaser, O. G. Schmidt, D. G. Cahill, N. Mingo, A. Rastelli, Role of surface-segregation-driven intermixing on the thermal transport through planar Si/Ge superlattices. *Phys. Rev. Lett.* **111**, 115901 (2013).

20. W. Kim, S. L. Singer, A. Majumdar, D. Vashaee, Z. Bian, A. Shakouri, G. Zeng, J. E. Bowers, J. M. O. Zide, A. C. Gossard, Cross-plane lattice and electronic thermal conductivities of ErAs:InGaAs/InGaAlAs superlattices. *Appl. Phys. Lett.* **88**, 242107 (2006).

21. M. L. Lee, R. Venkatasubramanian, Effect of nanodot areal density and period on thermal conductivity in SiGe/Si nanodot superlattices. *Appl. Phys. Lett.* **92**, 053112 (2008).

22. G. Pernot, M. Stoffel, I. Savic, F. Pezzoli, P. Chen, G. Savelli, A. Jacquot, J. Schumann, U. Denker, I. Mönch, Ch. Deneke, O. G. Schmidt, J. M. Rampnoux, S. Wang, M. Plissonnier, A. Rastelli, S. Dilhaire, N. Mingo, Precise control of thermal conductivity at the nanoscale through individual phonon-scattering barriers. *Nat. Mater.* **9**, 491–495 (2010).

23. S. Adachi, *GaAs and Related Materials: Bulk Semiconducting and Superlattice Properties* (World Scientific, 1994).

24. P. Sheng, *Introduction to Wave Scattering, Localization, and Mesoscopic Phenomena* (Springer, 2006).

25. J. Mendoza, G. Chen, Anderson localization of thermal phonons leads to a thermal conductivity maximum. *Nano Lett.* **16**, 7616–7620 (2016).

26. W. Zhang, T. S. Fisher, N. Mingo, The atomistic Green's function method: An efficient simulation approach for nanoscale phonon transport. *Numer. Heat Tr. B Fund.* **51**, 333–349 (2007).

27. A. MacKinnon, B. Kramer, One-parameter scaling of localization length and conductance in disordered systems. *Phys. Rev. Lett.* **47**, 1546–1549 (1981).

28. P. A. Lee, T. V. Ramakrishnan, Disordered electronic systems. *Rev. Mod. Phys.* **57**, 287–337 (1985).

29. P. W. Anderson, Absence of diffusion in certain random lattices. *Phys. Rev.* **109**, 1492–1505 (1958).

30. T. R. Kirkpatrick, Localization of acoustic waves. *Phys. Rev. B* **31**, 5746–5755 (1985).

31. A. Ioffe, A. Regel, Non-crystalline, amorphous, and liquid electronic semiconductors. *Prog. Semicond.* **4**, 237–291 (1960).

32. P. Sheng, M. Zhou, Z-Q. Zhang, Phonon transport in strong-scattering media. *Phys. Rev. Lett.* **72**, 234–237 (1994).

33. R. Venkatasubramanian, Lattice thermal conductivity reduction and phonon localization like behavior in superlattice structures. *Phys. Rev. B* **61**, 3091–3097 (2000).

34. M. V. Simkin, G. D. Mahan, Minimum thermal conductivity of superlattices. *Phys. Rev. Lett.* **84**, 927–930 (2000).

35. P. Sheng, M. Zhou, Heat conductivity of amorphous solids: Simulation results on model structures. *Science* **253**, 539–542 (1991).

36. I. Savić, N. Mingo, D. A. Stewart, Phonon transport in isotope-disordered carbon and boron-nitride nanotubes: Is localization observable? *Phys. Rev. Lett.* **101**, 165502 (2008).

37. C. Colvard, R. Merlin, M. V. Klein, A. C. Gossard, Observation of folded acoustic phonons in a semiconductor superlattice. *Phys. Rev. Lett.* **45**, 298–301 (1980).

38. Y. K. Koh, D. G. Cahill, Frequency dependence of the thermal conductivity of semiconductor alloys. *Phys. Rev. B* **76**, 075207 (2007).

39. K. T. Regner, D. P. Sellan, Z. Su, C. H. Amon, A. J. H. McGaughey, J. A. Malen, Broadband phonon mean free path contributions to thermal conductivity measured using frequency domain thermoreflectance. *Nat. Commun.* **4**, 1640 (2013).

40. C. Kadow, S. B. Fleischer, J. P. Ibbetson, J. E. Bowers, A. C. Gossard, J. W. Dong, C. J. Palmstrøm, Self-assembled ErAs islands in GaAs: Growth and subpicosecond carrier dynamics. *Appl. Phys. Lett.* **75**, 3548–3550 (1999).

41. M. J. Hÿtch, E. Snoeck, R. Kilaas, Quantitative measurement of displacement and strain fields from HREM micrographs. *Ultramicroscopy* **74**, 131–146 (1998).

42. M. J. Hÿtch, J.-L. Putaux, J.-M. Pénisson, Measurement of the displacement field of dislocations to 0.03 Å by electron microscopy. *Nature* **423**, 270–273 (2003).

43. M. Björck, G. Andersson, *GenX*: An extensible X-ray reflectivity refinement program utilizing differential evolution. *J. Appl. Crystallogr.* **40**, 1174–1178 (2007).

44. A. J. Schmidt, X. Chen, G. Chen, Pulse accumulation, radial heat conduction, and anisotropic thermal conductivity in pump-probe transient thermoreflectance. *Rev. Sci. Instrum.* **79**, 114902 (2008).

45. P. Giannozzi, S. Baroni, N. Bonini, M. Calandra, R. Car, C. Cavazzoni, D. Ceresoli, G. L. Chiarotti, M. Cococcioni, I. Dabo, A. Dal Corso, S. de Gironcoli, S. Fabris, G. Fratesi, R. Gebauer, U. Gerstmann, C. Gougoussis, A. Kokalj, M. Lazzeri, L. Martin-Samos, N. Marzari, F. Mauri, R. Mazzarello, S. Paolini, A. Pasquarello, L. Paulatto, C. Sbraccia, S. Scandolo, G. Sclauzero, A. P. Seitsonen, A. Smogunov, P. Umari, R. M. Wentzcovitch, QUANTUM ESPRESSO: A modular and open-source software project for quantum simulations of materials. *J. Phys. Condens. Matter* **21**, 395502 (2009).

46. J. P. Perdew, A. Zunger, Self-interaction correction to density-functional approximations for many-electron systems. *Phys. Rev. B* **23**, 5048–5079 (1981).

47. K. Esfarjani, G. Chen, H. T. Stokes, Heat transport in silicon from first-principles calculations. *Phys. Rev. B* **84**, 085204 (2011).

48. D. A. Broido, M. Malorny, G. Birner, N. Mingo, D. A. Stewart, Intrinsic lattice thermal conductivity of semiconductors from first principles. *Appl. Phys. Lett.* **91**, 231922 (2007).

49. M. P. Lopez Sancho, J. M. Lopez Sancho, J. M. L. Sancho, J. Rubio, Highly convergent schemes for the calculation of bulk and surface Green functions. *J. Phys. F Met. Phys.* **15**, 851 (1985).

50. R. M. Costescu, M. A. Wall, D. G. Cahill, Thermal conductance of epitaxial interfaces. *Phys. Rev. B* **67**, 054302 (2003).

51. J. P. Feser, D. G. Cahill, Probing anisotropic heat transport using time-domain thermoreflectance with offset laser spots. *Rev. Sci. Instrum.* **83**, 104901 (2012).

52. J. Yang, E. Ziade, A. J. Schmidt, Uncertainty analysis of thermoreflectance measurements. *Rev. Sci. Instrum.* **87**, 014901 (2016).

Citation: M. N. Luckyanova, J. Mendoza, H. Lu, B. Song, S. Huang, J. Zhou, M. Li, Y. Dong, H. Zhou, J. Garlow, L. Wu, B. J. Kirby, A. J. Grutter, A. A. Puretzky, Y. Zhu, M. S. Dresselhaus, A. Gossard, G. Chen, Phonon localization in heat conduction. *Sci. Adv.* **4**, eaat9460 (2018).

Science Advances

Phonon localization in heat conduction

M. N. Luckyanova, J. Mendoza, H. Lu, B. Song, S. Huang, J. Zhou, M. Li, Y. Dong, H. Zhou, J. Garlow, L. Wu, B. J. Kirby, A. J. Grutter, A. A. Puretzky, Y. Zhu, M. S. Dresselhaus, A. Gossard and G. Chen

ARTICLE TOOLS	http://advances.sciencemag.org/content/4/12/eaat9460
SUPPLEMENTARY MATERIALS	http://advances.sciencemag.org/content/suppl/2018/12/17/4.12.eaat9460.DC1
REFERENCES	This article cites 50 articles, 6 of which you can access for free http://advances.sciencemag.org/content/4/12/eaat9460#BIBL
PERMISSIONS	http://www.sciencemag.org/help/reprints-and-permissions

Use of this article is subject to the Terms of Service